Scanning-Raman-Microscopy for the Statistical Analysis of Covalently Functionalized Graphene

Jan M. Englert, Philipp Vecera, Kathrin C. Knirsch, Ricarda A. Schäfer, Frank Hauke, and Andreas Hirsch*

Department of Chemistry and Pharmacy and Institute of Advanced Materials and Processes (ZMP), University of Erlangen-Nuremberg, Henkestrasse 42, 91054 Erlangen, Germany

ABSTRACT We report on the introduction of a systematic method for the quantitative and reliable characterization of covalently functionalized graphene based on Scanning-Raman-Microscopy (SRM). This allows for recording and analyzing several thousands of Raman spectra per sample and straightforward display of various Raman properties and their correlations with each other in histograms or coded 2D-plots. In this way, information about the functionalization efficiency of a given reaction, the reproducibility of the statistical analysis, and the sample homogeneity can be easily deduced. Based on geometric considerations, we were also able to provide, for the first time, a correlation between the mean defect distance of densely packed point defects and the Raman I_D/I_G ratio directly obtained from the statistical analysis. This proved to be the prerequisite for determining the degree of functionalization, termed θ. As model compounds, we have studied a series of arylated graphenes (GPh) for which we have developed new synthetic procedures. Both graphite and graphene grown by chemical vapor deposition (CVD) were used as starting materials. The best route toward GPh consisted of the initial reduction of graphite with a Na/K alloy in 1,2-dimethoxyethane (DME) as it yields the highest overall homogeneity of products reflected in the widths of the Raman I_D/I_G histograms. The Raman results correlate nicely with parallel thermogravimetric analysis (TGA) coupled with mass spectrometry (MS) studies.

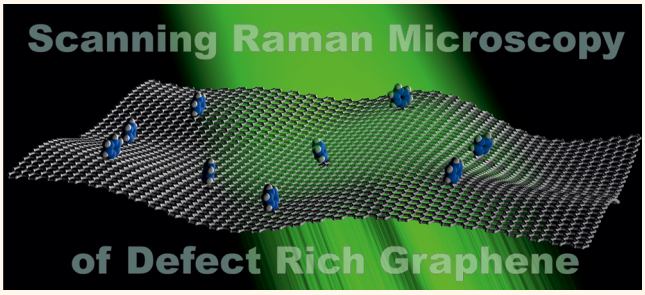

KEYWORDS: graphene · Raman · covalent functionalization · intercalation compounds · Raman statistics

Graphene is the youngest representative of synthetic carbon allotropes.[1−4] Its covalent addition chemistry has just recently begun to emerge.[5−26] Covalent graphene chemistry represents a very important and, at the same time, challenging subject.[6] Systematic investigations into graphene functionalization allow in principle for (a) the generation of decoupled monolayer sheets in large quantities, (b) the homogeneous dispersion and processing in solvents, (c) the combination of the outstanding properties of graphene with those of other compound classes, and (d) revealing the intrinsic chemical properties of this two-dimensional form of carbon. We have shown recently that graphite intercalation compounds (GICs), generated by reduction of graphite with alkaline metals, can easily be trapped with electrophiles such as diazonium salts[9] or alkylhalides[8] yielding covalently functionalized graphene. The advantage of this synthetic sequence is that the negatively charged graphene sheets in the GICs, whose most prominent representative possesses the chemical stoichiometry KC_8, are chemically activated. Additionally, in this GIC the graphene layers are already spatially decoupled and highly activated for follow-up-reactions such as electron transfer to and covalent addition of the organic addend. A similar approach, namely, bulk reduction and trapping with electrophiles has also been used to covalently functionalize single walled carbon nanotubes (SWCNTs) as demonstrated, for example, by the groups of Billups,[27] Tour,[28] and by our laboratory.[29] Compared with the reaction conditions used for the preparation of graphene oxide (GO),[30,31] the reductive route offers many advantages. Most importantly, the covalent functionalities are introduced without

* Address correspondence to andreas.hirsch@fau.de.

Received for review March 26, 2013 and accepted May 11, 2013.

Published online May 13, 2013
10.1021/nn401481h

disrupting the σ-framework of graphene, whereas during GO formation, the introduction of oxygen functionalities is accompanied by the formation of impossible-to-heal hole-defects caused by unwanted carbon loss through decarboxylation.[32,33] The most challenging aspect of covalent graphene chemistry is the structural characterization of the reaction products. In this regard, next to high resolution transmission electron microscopy,[34] and scanning probe techniques, Raman spectroscopy represents the most versatile method for the characterization of functionalized synthetic carbon allotropes.[35−39] Compared to scanning probe microscopy (SPM), which allows very high spatial resolution well below the optical diffraction limit, SRM naturally provides faster areal coverage, however, sacrificing locality of the spectral information obtained. Hybrid forms of SPM and Raman are currently entering the field based on scanning near field optical microscope (SNOM) technology. In conjunction with Raman spectroscopy, such techniques are termed tip enhanced Raman scattering (TERS). These setups combine the high spatial resolution of the scanning probe microscopy with the spectral information obtained from Raman measurements. Conventional Raman microscopy allows for the determination of defect densities,[40,41] aggregation or exfoliation states,[42] doping and electronic properties.[38,43,44] In particular, the analysis of the defect induced band (D-band) and its double frequency overtone (2D-band) allows retrieving information on generated sp^3-defects (D-band) and exfoliation of individual graphene sheets (2D-band) leading to electronic decoupling. However, one has to keep in mind that a single Raman spectrum is only a spot test and can easily imply misleading results since information is obtained locally with optical resolution. Sample homogeneity, however, usually cannot be ensured within these length scales. Furthermore, as an emissive technique, point spectra always reflect the "brightest", hence most effective, Raman scatterer at the measurement position which might not necessarily coincide with the sample's most abundant specimen. In the case of covalent SWCNT chemistry, similar problems arise. For this reason, we have recently introduced SRM for the statistical analysis of covalently functionalized SWCNTs.[45] The success of this method is based on the systematic analysis of several thousands of spatially resolved Raman point spectra per sample. Based on the resulting data set, we introduced three Raman-indices, namely, the Raman Defect Index (RDI), Raman Homogeneity Index (RHI) and Raman Selectivity Index (RSI), which quantify the density of defects, the sample homogeneity, and the electronic type selectivity of a given covalent SWCNT functionalization reaction. Now we introduce a related Scanning-Raman-Microscopy treatment for the characterization of covalently functionalized graphene. This offers a very clear and quantitative picture of the outcome of covalent graphene chemistry and also allows for the first time to directly deduce the degree of functionalization θ of covalent graphene adducts. This is demonstrated by the introduction of a new reaction sequence for the formation of polyarylated graphene (GPh). These adducts were generated by reducing graphite under modified *Birch*-conditions or by the direct treatment with potassium, followed by trapping of the negatively charged graphene sheets with phenyl iodide. The process is very efficient and can be scaled up, and the degree of functionalization is tunable depending on the applied reaction conditions.

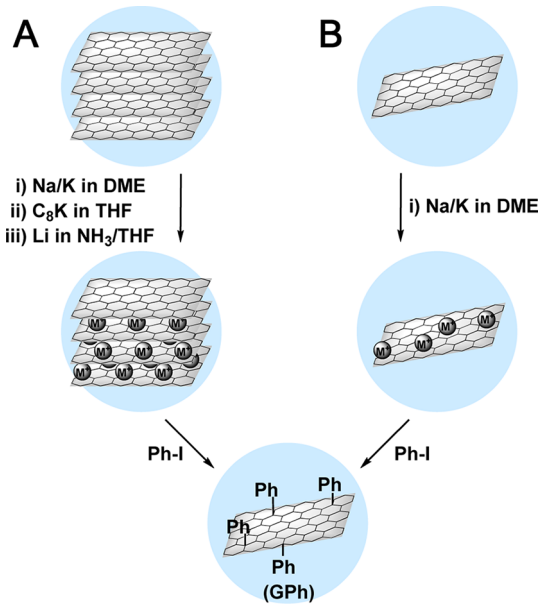

Scheme 1. Synthesis of arylated graphene GPh. (A) Reductive bulk arylation: method-*i* (GPh-*i*), 5 mmol Na/K alloy in 150 mL DME, 1 mmol C, quenched with an excess of PhI; method-*ii* (GPh-*ii*), dissolution of 20 mg KC_8 in 100 mL THF, quenched with an excess of PhI; method-*iii* (GPh-*iii*), liquid NH_3/THF 1:1 (200 mL), 1 mmol C, 5 mmol lithium, −78 °C, quenched with an excess of PhI. (B) Reductive arylation on CVD grown graphene transferred to Si/SiO_2 by a modification of method-*i*.

RESULTS AND DISCUSSION

To develop a simple and nondestructive method for the synthesis of covalently functionalized graphene to be analyzed by SRM, we decided to arylate reduced graphite or graphene *via* the treatment with phenyl iodide as a mild electrophile. So far arylation was mainly achieved with either benzoylperoxides[46] or diazonium chemistry.[6,9,11] We have applied a series of different exfoliation and activation routes and next to graphite (Scheme 1A), we have also used CVD-graphene (Scheme 1B) as starting material. As graphite source spherical graphite (SGN18) was used, which proved beneficial due to its high surface area (SEM and TGA characterization available in the Supporting Information, Figure S1a,b). Exfoliation and reduction was accomplished either by treatment with the liquid sodium/potassium alloy with the composition NaK_3 in DME

(method-*i*), solid potassium (method-*ii*) or lithium dissolved in a mixture of liquid ammonia and tetrahydrofuran (THF) (method-*iii*). The variation of the reaction conditions (methods *i*–*iii*, Scheme 1A) allowed us to investigate the influence of parameters such as the nature of the alkali metal and the solvent on the efficiency of the arylation reaction. The subsequent treatment of these reaction mixtures with phenyl iodide led to a color change of the dispersion from blue to a homogeneous black.

In method-*ii*, a first stage potassium GIC of SGN18 was synthesized and subsequently treated with phenyl iodide after being dissolved in absolute THF by brief ultrasonication treatment. All samples were washed during the workup in order to remove salts and other byproducts. Finally, the desired arylated compounds GPh-*i*–*iii* were obtained.

To gain insight into whether the functionalization was successful, we characterized bulk samples of all GPhs with TGA-MS. It was hence possible to unambiguously identify the fragments cleaved from the products of the reaction (Figure 1). These investigations proved the attachment of the phenyl groups through detection of the PhH^+ fragment $^m/_z = 78$.

In direct comparison between GPh-*ii* and GPh-*iii*, we found the higher mass loss for GPh-*iii*, which lost 14.2% during the treatment while GPh-*ii* only lost 10.6%.

In the series of all samples, GPh-*i* exhibited the highest mass loss of 15.8%. If arylation is considered as exclusive functionalization, mass loss can be converted into molar addend loss by dividing it through the recorded mass of the cleaved fragment. Consequently, the TGA degree of functionalization can be calculated as the ratio between the moles of cleaved addend and the moles of carbon left. Using this procedure, a TGA degree of functionalization of 2.9% is obtained for GPh-*i*, while GPh-*ii* and GPh-*iii* were found to display 1.8% and 2.6% of functionalization, respectively.

We now turn to the Raman spectroscopic characterization of the arylation products GPh-*i*–*iii* and first focus our attention on the dispersive D-band, which appears at 1345 cm^{-1} for a laser excitation wavelength of 532 nm. This band is particularly useful because it is forbidden by selection rules in the absence of a scattering site to relax the fundamental $q \sim 0$ Raman rule.[44,47–50] This is not the case for the always allowed Γ-point phonon emission responsible for the G-band at ~1582 cm^{-1} and also for most of the higher order overtones which deliver wavevector/pseudomomentum conservation through forward/backward scattering.[42] To use Raman spectroscopy for quantification of the density of defects, one needs to relate the D-band intensity I_D to the amount of defects per area which is usually done by comparing it to the G-band intensity I_G. This comparison is feasible because I_G is proportional to the amount of carbon atoms illuminated in the area of the laser spot and remains almost constant for a single graphene layer until a certain threshold of

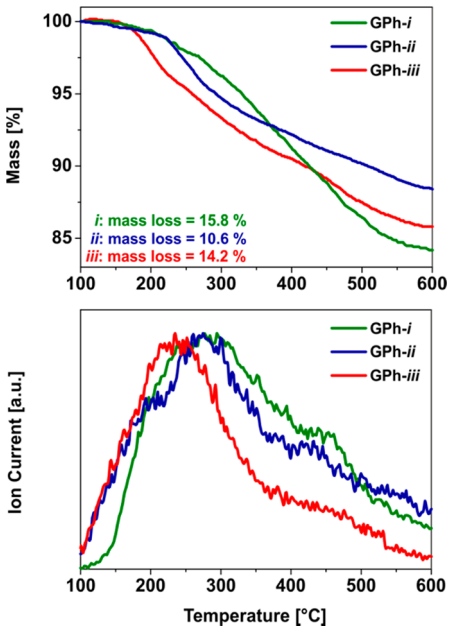

Figure 1. (Top) TGA-MS data of the bulk samples GPh-*i*–*iii*. The corresponding mass losses are 15.8% (GPh-*i*), 10.6% (GPh-*ii*) and 14.2% (GPh-*iii*) between 100 and 600 °C. (Bottom) Recorded ion current for $^m/_z = 78$ as a function of furnace temperature elucidating the presence of the covalently bound phenyl addends. Reference material measured with the same temperature ramp can be found in the Supporting Information.

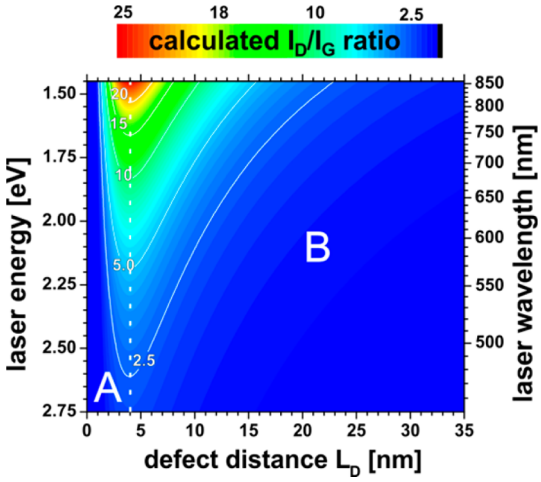

Figure 2. Generalized correlation between calculated I_D/I_G Raman ratio, mean defect distance L_D and laser energy or wavelength. The region marked with "A" left to the dashed white line is denoted as high region of low density of defects, while the region marked with "B" is referred to as low defect density region.

defects at a mean interdefect distance (L_D) is reached at about 3 nm[40] depending on the applied excitation laser wavelength as visualized in Figure 2. Following these considerations, Cançado and Lucchese developed a model[40,41] to relate the interdefect distance to the I_D/I_G ratio which we generalized and summarized in Figure 2.

In essence it is important to understand that an increase of the I_D/I_G ratio is not necessarily correlated

with a decrease of the interdefect distance or equivalently, an increase of the density of functionalization. Every I_D/I_G ratio can be assigned to two different L_D values (Figure 2), either on the high- or on the low density of defects side of the relation's maximum. Keeping these fundamental considerations in mind, it is furthermore important to realize that Raman investigations in the solid state are always accompanied by possible morphological reorganization processes caused by drying or surface deposition procedures. These can lead to rather inhomogeneous samples in terms of morphology which is clearly reflected in the Raman spectra. As a consequence, single Raman spectra taken at a certain location are not suitable to characterize a sample sufficiently. No spatially resolved and statistically significant information is provided in this way since a single spectrum cannot reflect the entire sample composition. Consequently, more representative routines have to be used. If, for example, the sample under consideration consists not only of monolayers but also of few layers, the superposition of functionalized with unfunctionalized areas breaks the simple proportionality of the G-band intensity with the amount of carbon atoms per illuminated area. Now, sample volume, transmission/reflection and absorption of excitation light from and into lower layers play an increasingly important role. Nevertheless, Raman spectroscopy is still the most powerful tool to determine key characteristics of the bulk sample under consideration when compared to the starting material. Mean degrees of Raman functionalization, functionalization homogeneity and the width of a I_D/I_G histogram can straightforwardly be extracted from a data set with high reliability and reproducibility as demonstrated in Figure 3.

We now present in more detail the SRM results obtained for all three bulk samples GPh-*i*−*iii* and compare them with the starting material. On average, no less than 10 000 point spectra were collected from each sample. These raw data can be fitted to extract key characteristics for every point spectrum like the I_D/I_G ratio, the 2D-band intensity and the full width at half magnitude (fwhm) of the D- or 2D-band. Those values can be correlated with each other, *e.g.*, the evolution of the G-band intensity as a function of I_D/I_G ratio or might just be shown as a distribution histogram. Such graphical representations of the data clearly reflect the big advantage of the statistical analysis. For example, successful functionalization becomes apparent at first glance by looking at the maxima of the I_D/I_G distributions in the corresponding histograms seen in Figure 4. The relative D-band intensity is a measure for the amount of sp^3-defects in the sp^2-hybridized graphene/graphite lattice.[40,41] The pristine starting material exhibits an almost perfect Gaussian distribution of the I_D/I_G values with a very low standard deviation σ of 0.06 (Figure 4), a consequence of the homogeneity of the pristine material and the low slope of the curve in

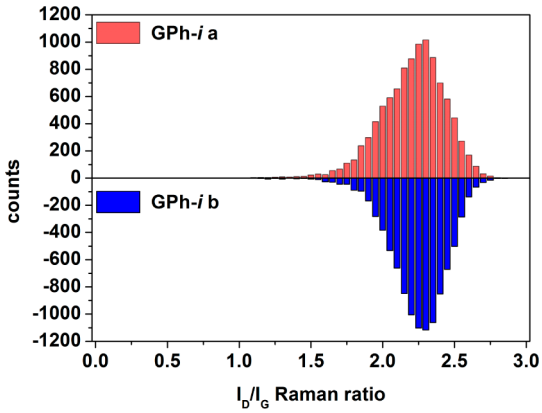

Figure 3. Randomized statistical measurement of the Raman I_D/I_G ratios of GPh-*i* measured at two different positions (a and b). Comparison of the histograms reflects the reliability and reproducibility of the statistical analysis.

Figure 2 in the regime of low mean defect distances. It also exhibits the typical narrow D- and G-bands and the asymmetrical shape of the 2D-band as expected for the Bernal AB stacked crystalline graphite. After functionalization, all histograms present a shift of the histogram maximum to higher mean I_D/I_G ratios than those of the pristine reference material. This, in general, indicates the formation of an arbitrary amount of sp^3-defects and hence a successful covalent arylation in the first place. However, recalling the evolution of the I_D/I_G ratio as a function of mean defect distance L_D, as depicted in Figure 2, a lower I_D/I_G ratio does not categorically indicate a lower density of defects. The reason for this unintuitive behavior is found in the curve shape of Figure 2, which proceeds through a maximum at mean defect distances at around 3 nm and decreases to both directions, for higher and lower mean defect distances. The mean spectral shape determined for GPh-*ii* and GPh-*iii* (Figure 4) is very reminiscent to defect-rich, nanocrystalline graphite and for all shown samples no longer permits layer quantification by 2D-band shape or intensity analysis. The loss in structure in the second order spectrum is a result of averaging the manifold of differently layered small stacks during the mapping procedure. The mean spectrum shown is calculated from all these individual spectra and hence must also reflect this spectral diversity by strong suppression of intense and sharp characteristic features in this spectral region due to the expected fluctuations and inhomogeneity in the sample. The high density of defects present in GPh-*ii* and GPh-*iii* becomes evident when comparing the width of the first order Raman bands, especially the D- and G-band, with those of the pristine starting material in Figure 4, as suggested earlier for the shape of D-band.[40] We added the G-band shape to the analysis, as in GPh-*ii* and GPh-*iii* the increased G-band width is a consequence of the merging of the G-band with the G′-band, a defect activated, close relative to the D-band which originates from a zone center intravalley process

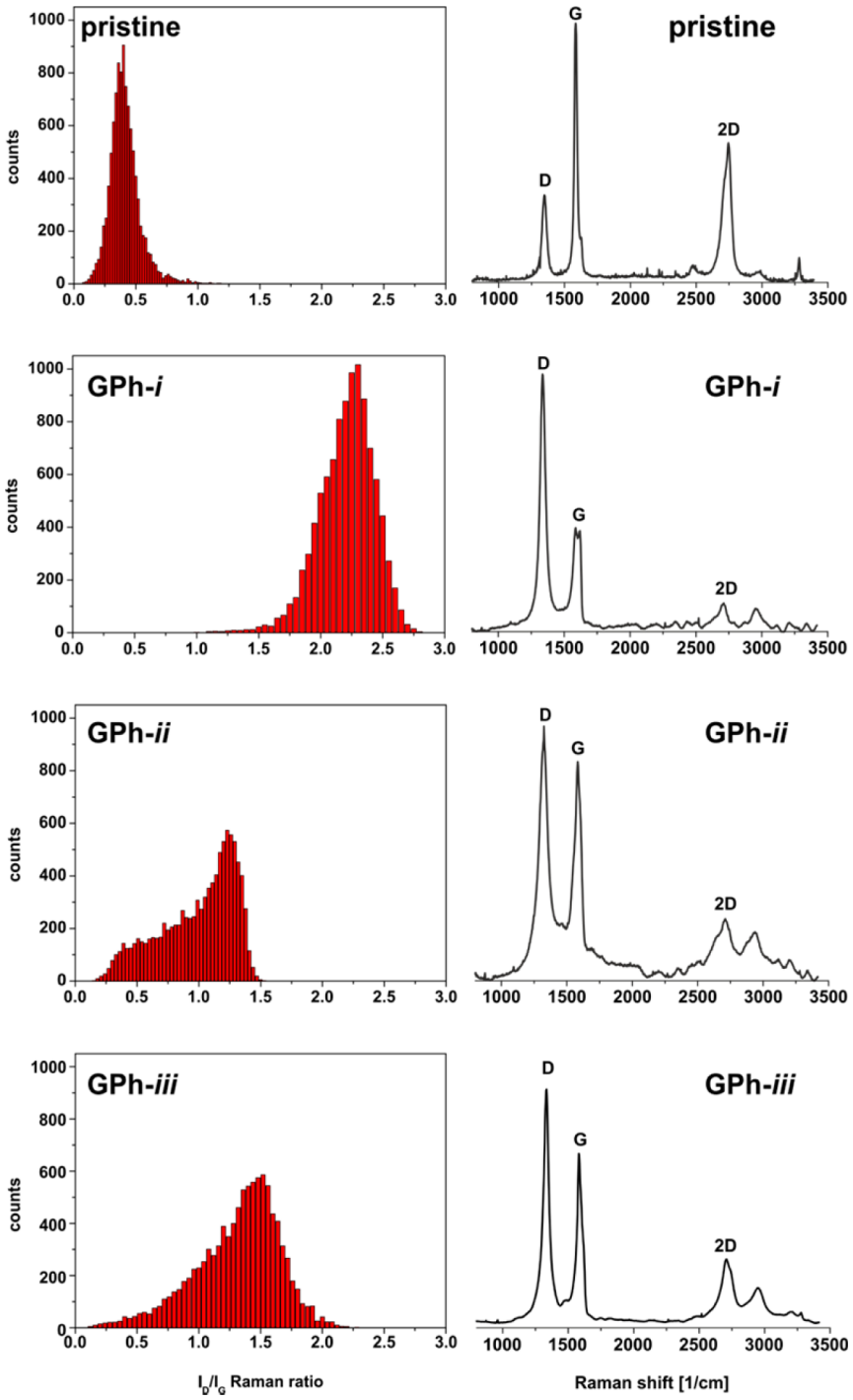

Figure 4. (Left) Histograms of the I_D/I_G frequencies recorded from large area (min. 100 × 100 μm^2) Raman measurements of GPh-*i*−*iii* and the starting material SGN18 spherical graphite. (Right) Average spectra calculated from the complete data set (mean spectra) displaying the typical D-, G- and 2D-band signals.

with small wavevector compared to the intervalley D-band signal, that is attributed to a zone boundary phonon.[42,44,48] The resulting G-band feature is composed of both signals, G- and G′-band, which leads to an overall broadening of the signal as a consequence of the high functionalization present in GPh-*ii* and GPh-*iii*. The same band can be seen in GPh-*i* (and also faintly in the pristine material) but the intensity and width is so small that the signal appears only as a shoulder or a sideband at the high energy flank of the G-band effectively producing a resolved double peak—a clear indication for a lower density of functionalization compared to GPh-*ii* and GPh-*iii* even though their histogram maximum positions are found at lower I_D/I_G values when compared to GPh-*i*. Furthermore, a strong broadening of the histogram may be induced through the sample sitting on the steep slope of the high density functionalization side A of the function in Figure 2.

In summary, for the arylation products GPh-*ii* and GPh-*iii*, we conclude that the samples must be assigned to the high density of defects region judging from the mean spectral shape and from the broad distribution in the corresponding histograms. For GPh-*i*, the mean spectral shapes for the D-, G- and G′-band together with the histogram suggest that the sample obtains values near the maximum of reachable values for I_D/I_G ratios at this excitation wavelength. The question whether it is attributed to the high or the low density of defects regime is answered in favor of the high density of defects regime as the low density side is expected to present better resolved separation between the G- and the G′-band.[40]

In the case of GPh-*i*, a good match of the TGA degree of functionalization of 2.9% was obtained with the Raman measurements where a sample with a mean I_D/I_G ratio of 2.25 on the high density functionalization side corresponds, according to Figure 2, to a mean defect distance (L_D) of 1.74 nm, while a L_D of 1 nm is expected from the TGA results. The corresponding L_D evaluation has not been conducted for the products of arylation termed GPh-*ii*−*iii* because they are too inhomogeneous. The same Raman-analysis is carried out for the CVD-grown monolayer graphene functionalized in analogy to method-*i* (Scheme 1B) for comparison. This material was investigated as a deposit on Si/SiO_2. The experiment turned out to be the perfect showcase as the material is strictly of monolayer nature, very homogeneous and very flat on scales relevant for the SRM measurements. The presence of the intense and symmetric 2D-band in the mean Raman spectrum presented in Figure 5, before and after functionalization, clearly demonstrates the single layer nature and its preservation.

As can be seen in the color-coded Raman maps shown in Figure 6, an increase of the overall D-band intensity takes place after applying this mild reaction sequence. The Raman frequency histogram plotted next to the color coded maps clearly represents the outcome of the reaction, however, without displaying spatially resolved information.

As judged from the spectral shape and intensity in the 2D-band region (Figure 5) in comparison to values obtained from ion bombarded samples,[40,41] it became clear that the L_D values remained above 5 nm for this reaction. In this data interval, the conversion from the measured I_D/I_G ratios to mean defect distance L_D can be deduced using eq 1, which was obtained from a curve simulation of the published data.[40] The exact fitting parameters for the exponentially decaying part of the relation obtained from Cançado *et al.* can be found in the Supporting Information (S2).

$$L_D[\mathrm{nm}] = \sum_{i=0}^{2} A_i e^{-[(I_D/I_G)/b_i]} + A_3 \qquad (1)$$

The result of the spatial mapping is presented in the second contour plot in Figure 6. The histogram reveals

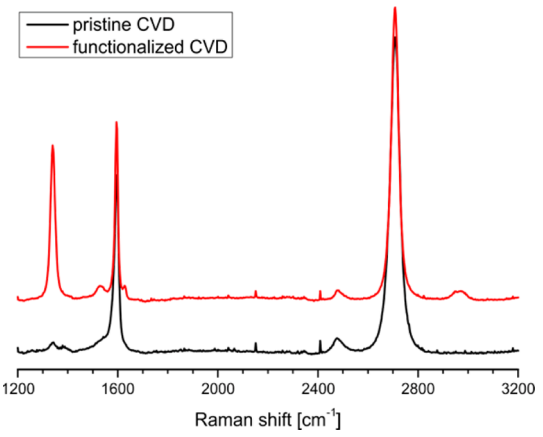

Figure 5. Mean Raman spectra of the pristine and the reductively arylated CVD graphene on Si/SiO_2.

a mean distance between two addends of about 12 nm. From this defect distance the degree of functionalization can be derived by a simple calculation taken the following considerations into account.

Anticipating a dense and isotropic packing of defects in the graphene lattice one may assume a situation like that depicted in Figure 7. The area per defect A_{Def} is calculated from the L_D measurements in order to correlate it to the number of affected carbon atoms. Hence, it represents the Raman degree of functionalization. For quantification, the area per carbon atom A_C is needed eq 2 and easily deduced from the hexagonal lattice constants. Due to the diatomic basis of graphene, it is given as half of the area of the graphene unit cell defined by the two graphene lattice vectors $\mathbf{a}_1$ and $\mathbf{a}_2$ covering an angle of $\alpha = 60°$.

$$A_C = |a|^2 \frac{\sqrt{3}}{4} \qquad (2)$$

If we now consider that the area per defect A_{Def}, eq 3 and 4, is just the area of the circle around the point defect (A_O) plus twice the fraction of the residue A_R (hatched area in Figure 7) between the circles

$$A_{Def} = A_O + 6\frac{A_R}{3} \qquad (3)$$

$$A_{Def} = L_D^2 \frac{\pi}{4} + 2A_R \qquad (4)$$

we obtain the degree of functionalization θ eq 5 by calculating θ as the ratio between

$$\theta = \frac{1}{\left(\frac{A_{Def}}{A_C} - 1\right)} \approx \frac{A_C}{A_{Def}} \qquad (5)$$

which can be simplified for the case when A_{Def} is significantly larger than A_C. The unknown area A_R can be found as the area spanned from the triangle between three defects A_Δ minus three times the gray circle segment A_{seg}, eqs 6−8.

$$A_R = A_\Delta - 3A_{seg} \qquad (6)$$

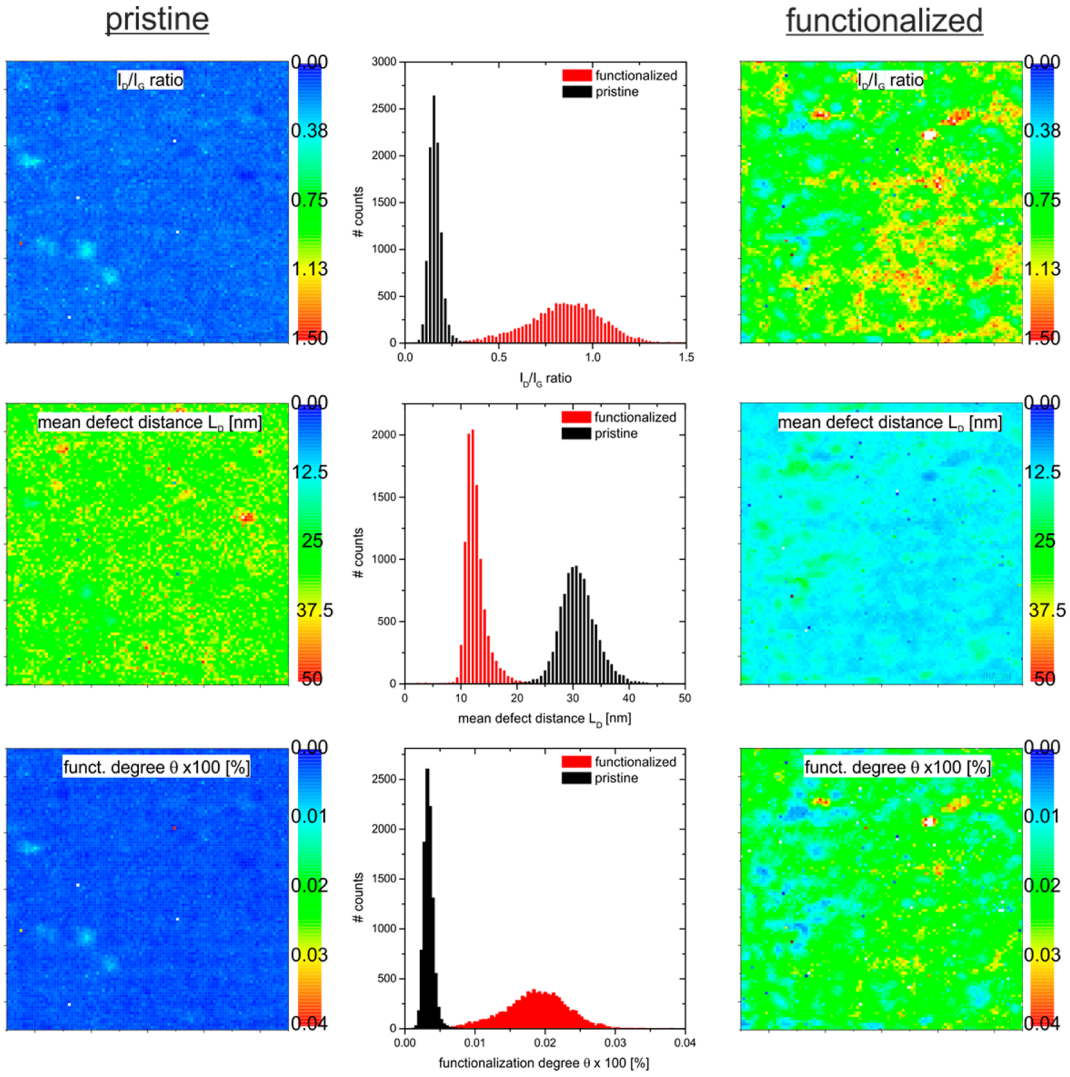

Figure 6. Spatial and histogram representation of the I_D/I_G ratio, the mean L_D defect distance values and the resulting degree of functionalization; (left) spatial mappings of the properties before functionalization; (middle) histogram representation of the value distribution in the spatial mappings; (right) spatial mappings of the properties after functionalization.

$$A_R = L_D^2\frac{\sqrt{3}}{4} - L_D^2\frac{\pi}{8} \tag{7}$$

$$A_R = L_D^2\frac{2\sqrt{3}-\pi}{8} \tag{8}$$

Substituting A_R in the expression for A_{Def} now leads to eqs 9 and 10

$$A_{Def} = L_D^2\left(\frac{\pi}{4}+\frac{2\sqrt{3}-\pi}{4}\right) \tag{9}$$

$$A_{Def} = L_D^2\frac{\sqrt{3}}{2} \tag{10}$$

which is just two times A_Δ. The degree of functionalization θ is then reduced to only fundamental lengths, eq 11:

$$\theta = \frac{a^2}{2L_D^2} \tag{11}$$

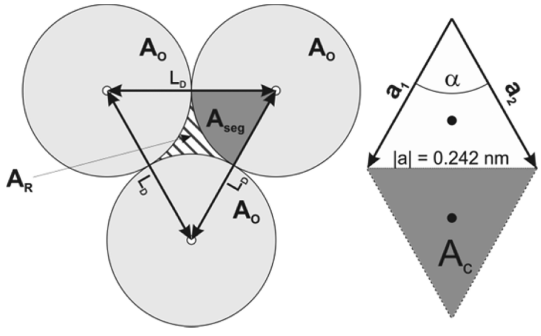

Figure 7. (Left) Model for a dense packing of isotropically distributed defects (small open circles) separated by a distance L_D and surrounded by the area A_O. (Right) Graphene unit cell with lattice vectors a_1 and a_2; the shaded area A_C is attributed to a single carbon atom (right).

With this information at hand, it is possible to correlate θ with the measured I_D/I_G ratio at a given laser excitation (Figure 8).

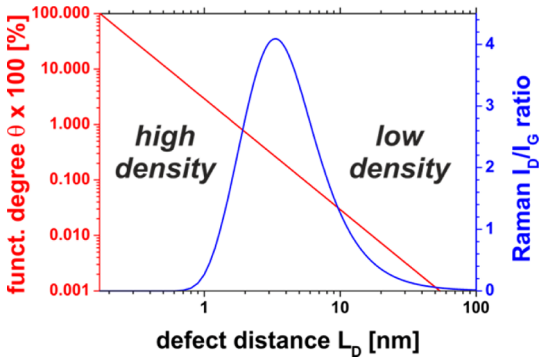

Figure 8. Correlation of L_D with degree of functionalization θ (log scale) in red and experimental I_D/I_G ratio in blue for 532 nm laser excitation. According to the definition from Figure 2, the areas left and right from the curve maximum are denoted as high- and low-defect density areas, respectively.

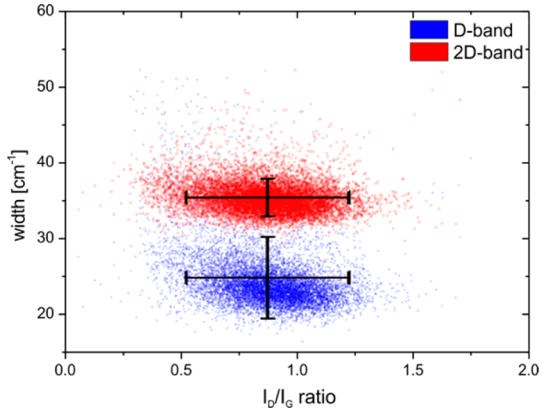

Figure 9. Scatter-plot of the spread of the D- and 2D-band width values as a function of I_D/I_G ratio for GPh-*i* on CVD graphene.

Thus, the mean distance of 12 nm for the functionalized CVD graphene (Figure 6) corresponds to a mean degree of functionalization of 0.02% assuming isotropic functionalization within the length scales accessible to the optical measurements (~1000 nm). To find a suitable criterion to discriminate high from low density functionalization, we analyzed the phenyl functionalized CVD grown graphene more closely. As most suitable criterion we chose the D-band width as it was reported to broaden for high density functionalization.[40] The D-band is not expected to be as sensitive as the 2D-band to other effects like doping or layer stacking, which in turn was found to be relatively unaffected by functionalization (Figure 5 and 9). Correlations between I_D/I_G ratio and the D-band width are graphically represented in Figure 9. As a result, we found a mean D-band width of $w(D) = 24.8 \pm 5.4$ cm^{-1} for $\lambda_{exc.} = 532$ nm.

Experimentally, two possible L_D-values may now be distinguished from each other by analyzing the spectral shape of the D-band. The latter is classified as either being below or above $w(D)_{max}$ ~30 cm^{-1}. For the CVD functionalized sample, this value was always found to be smaller than the $w(D)_{max}$ ~30 cm^{-1}. Thus, below

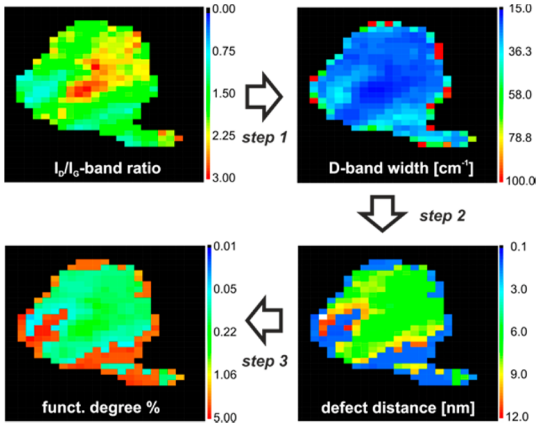

Figure 10. Stepwise sequence to obtain the degree of functionalization θ from a hexyl functionalized single layer graphene;[8] note that the last plot is given on a logarithmic color scale for better visualization.

a D-band width of 30 cm^{-1}, we attribute a recorded spectrum to be of low density functionalization (L_D > 3.5 nm), while a D-band width larger than 30 cm^{-1} stems from highly functionalized areas with L_D values <3.5 nm. For the latter region, the first equation can no longer be used to determine L_D from I_D/I_G values and must be replaced by the polynomial below eq 12, for fitting parameters, please see Supporting Information S1 and S2.

$$L_D[\text{nm}] = \sum_{i=0}^{8} a_i (L_D/I_G)^i \qquad (12)$$

To visualize the application of the final procedure, we used a hexyl functionalized sample from literature[8] (Figure 10). After fitting of the local D-band width (step 1), a successful splitting of the recorded data set into high- and low density of defects areas is carried out. A separate determination of the respective L_D values is then possible (step 2), and finally, calculation of the corresponding θ values from the reassembled overall L_D map is carried out (step 3). Hence, we were able to present the viability of our method for the calculation of the degree of functionalization not only for perfect, large areas of graphene, but also for flake samples derived from a bulk synthesis.

CONCLUSION

We have introduced a systematic method for the quantitative and reliable characterization of covalently functionalized graphene. For this purpose, we have used SRM, which allows us to record and analyze several thousands of Raman spectra per sample and to display various Raman properties and their correlations with each other in histograms or coded 2D-plots. We have carried out such statistical investigations with a series of arylated graphenes (GPh) for which we have developed new synthetic procedures. Both graphite and CVD grown monolayer graphene were used as starting materials. In this way, information about the

functionalization efficiency of a given reaction, the reproducibility of the statistical analysis, and the sample homogeneity can be easily deduced. Based on geometric considerations, we were also able to provide, for the first time, a correlation between the mean defect distance of densely packed point defects and the Raman I_D/I_G ratio directly obtained from the statistical analysis. This proved to be useful in determining the degree of functionalization θ of GPh including arylated CVD graphene. The best route toward arylated graphene consisted of the initial reduction of graphite with a Na/K alloy in DME as it leads to the highest overall homogeneity of products reflected by the widths of the Raman I_D/I_G histograms. The Raman results correlate very well with independent TGA-MS studies. The methods introduced here will be very useful and important for future graphene chemistry in general. Covalent functionalization of graphene has just started to develop, and next to the exploration of new synthesis protocols, the development of reliable characterization procedures is at least just as important.

METHODS

Raman Spectroscopy. Raman spectroscopic characterization was carried out on a Horiba Jobin Yvon LabRAM Aramis confocal Raman microscope (excitation wavelength: 532 nm) with a laser spot size of ~1 μm (Olympus LMPlanFl 100×, NA 0.80) in backscattering geometry. A silicon detector array charge coupled device (CCD) at −70 °C is used to record the spectrum. The spectrometer was calibrated in frequency using a diamond or crystalline graphite prior to measurement. Statistical Raman measurements were obtained through a motorized x-y table in a continuous linescan mode (SWIFT-module) in order to guarantee fast data acquisition. Initial data reduction and optimizations like baseline and noise corrections were performed directly inside the LabSpec 5 software. The spatially resolved spectroscopic information was further analyzed after export into OriginPro 8.6G software as 2D data matrices. All following arithmetic operations, statistic treatment, and graphics export were conducted within this software suite.

Thermogravimetric Analysis Combined with Mass Spectrometry (TGA-MS). Thermogravimetric analysis (TGA) equipped with a mass spectrometer (MS) was performed on a Netzsch STA 409 CD instrument equipped with a Skimmer QMS 422 mass spectrometer (MS/EI) with the following programmed time-dependent temperature profile: 24−700 °C with 10 K/min gradient and cooling to room temperature. The initial sample weights were about 5−10 mg, and the whole experiment was executed under inert gas atmosphere with a He gas flow of 80 mL/min.

Procedure Used for the Preparation of Arylated CVD Graphene. Inside of a glovebox (<0.1 ppm O_2, <1 ppm H_2O, Argon atmosphere), a liquid Na/K alloy was prepared by melting 3.9 mmol Na and 7.7 mmol K at 70 °C. The alloy was then added to 20 mL of fresh distilled and degassed 1,2-DME and stirred 12 h to give a deep blue solution. One drop of this solution was dropped on a 1 × 1 cm^2 CVD graphene sheet on a 90 nm SiO_2/Si wafer. Afterwards, a drop of phenyl iodide was added. The wafer was removed from the glovebox after 1 h reaction time and washed twice with 2-propanol and once with acetone. Finally, it was dried at 70 °C for 3 h.

Procedure Used for the Preparation of GPh-*i*. Under argon atmosphere, 0.45 mL of a freshly prepared, liquid Na/K alloy (3.9 mmol Na and 7.7 mmol K for an eutectic mixture) in 150 mL of 1,2-DME (freshly distilled over Na/K) was stirred in a flame-dried round-bottom flask at room temperature. After a short ultrasonic pulse, 24 mg (2.0 mmol carbon) of spherical graphite SGN18 was added to the deep-blue solution and stirred for three days, before the reaction mixture was treated with 6 equiv of phenyl iodide (1.35 mL, 12 mmol) and stirred overnight.

Procedure Used for the Preparation of GPh-*ii*. Inside of a glovebox (<0.1 ppm O_2, <1 ppm H_2O, Argon atmosphere), 240 mg (20 mmol carbon) of spherical graphite SGN18 and 98 mg (2.5 mmol) of potassium were heated to 200 °C in a glass bottle. The mixture was stirred and heated at 200 °C, until the reaction was finished. After the formation of the first stage K GIC, the powder was allowed to cool to ambient temperature before it was dissolved in absolute THF (0.2 mg/mL) by brief ultrasonication. Subsequently, the dispersion was treated with 6 equiv of phenyl iodide (1.35 mL, 12 mmol) and stirred overnight.

Procedure Used for the Preparation of GPh-*iii*. In a flame-dried and argon purged, four-necked, round-bottomed flask (250 mL) equipped with two gas inlets and pressure compensation, 100 mL of anhydrous THF (<5 ppm H_2O) was cooled to −78 °C and ammonia (100 mL) was condensed. After the addition of 5 equiv of lithium (35 mg, 5.0 mmol), a deeply blue colored solution was formed wherein 12 mg (1.0 mmol carbon) of spherical graphite SGN18 was added. After stirring for 1 h, a blue-black dispersion was obtained and the cooling was removed. After complete evaporation of ammonia, the remaining lithium-bronze was removed by a syringe and the dispersion was ultrasonicated for 20 min in a bath type sonicator. Arylation was achieved by treatment with 6 equiv of phenyl iodide (1.35 mL, 12 mmol) and stirring overnight.

Final Workup of Arylation GPh-*i*−*iii*. Lithium, sodium and potassium salts as well as the excess of the interception reagent were removed by transferring into a separation funnel charged with cyclohexane (100 mL) and copious washing with distilled water (200 mL). The organic layer containing the carbonaceous material was filtered through a 0.2 μm reinforced cellulose membrane filter (Sartorius) and thoroughly washed with THF, 2-propanol, ethanol and water (50 mL each). The resulting black solid was dried at 70 °C overnight.

Conflict of Interest: The authors declare no competing financial interest.

Acknowledgment. The authors thank the Deutsche Forschungsgemeinschaft (DFG-SFB 953 "Synthetic Carbon Allotropes", Project A1), the Interdisciplinary Center for Molecular Materials (ICMM), the European Research Council (ERC; grant 246622 GRAPHENOCHEM), and the Graduate School Molecular Science (GSMS) for financial support.

Supporting Information Available: Experimental details and reference measurements. This material is available free of charge *via* the Internet at http://pubs.acs.org.

REFERENCES AND NOTES

1. Geim, A. K. Graphene: Status and Prospects. *Science* **2009**, *324*, 1530–1534.
2. Geim, A. K.; Novoselov, K. S. The Rise of Graphene. *Nat. Mater.* **2007**, *6*, 183–191.
3. Novoselov, K.; Geim, A.; Morozov, S.; Jiang, D.; Zhang, Y.; Dubonos, S.; Grigorieva, I.; Firsov, A. Electric Field Effect in Atomically Thin Carbon Films. *Science* **2004**, *306*, 666–669.
4. Hirsch, A. The Era of Carbon Allotropes. *Nat. Mater.* **2010**, *9*, 868–871.
5. Chua, C. K.; Pumera, M. Covalent Chemistry on Graphene. *Chem. Soc. Rev.* **2013**, *42*, 3222–3233.
6. Hirsch, A.; Englert, J. M.; Hauke, F. Wet Chemical Functionalization of Graphene. *Acc. Chem. Res.* **2013**, *46*, 87–96.
7. Schäfer, R. A.; Englert, J. M.; Wehrfritz, P.; Bauer, W.; Hauke, F.; Seyller, T.; Hirsch, A. On the Way to Graphane-Pronounced Fluorescence of Polyhydrogenated Graphene. *Angew. Chem., Int. Ed.* **2012**, *52*, 754–757.

8. Englert, J. M.; Knirsch, K. C.; Dotzer, C.; Butz, B.; Hauke, F.; Spiecker, E.; Hirsch, A. Functionalization of Graphene by Electrophilic Alkylation of Reduced Graphite. *Chem. Commun.* **2012**, *48*, 5025–5027.
9. Englert, J. M.; Dotzer, C.; Yang, G.; Schmid, M.; Papp, C.; Gottfried, J. M.; Steinrück, H.-P.; Spiecker, E.; Hauke, F.; Hirsch, A. Covalent Bulk Functionalization of Graphene. *Nat. Chem.* **2011**, *3*, 279–286.
10. Malig, J.; Englert, J. M.; Hirsch, A.; Guldi, D. M. Wet Chemistry of Graphene. *Electrochem. Soc. Interface* **2011**, *16*, 53–56.
11. Huang, P.; Jing, L.; Zhu, H.; Gao, X. Diazonium Functionalized Graphene: Microstructure, Electric, and Magnetic Properties. *Acc. Chem. Res.* **2013**, *46*, 43–52.
12. Johns, J. E.; Hersam, M. C. Atomic Covalent Functionalization of Graphene. *Acc. Chem. Res.* **2013**, *46*, 77–86.
13. Park, J.; Yan, M. Covalent Functionalization of Graphene with Reactive Intermediates. *Acc. Chem. Res.* **2013**, *46*, 181–189.
14. Paulus, G. L. C.; Wang, Q. H.; Strano, M. S. Covalent Electron Transfer Chemistry of Graphene with Diazonium Salts. *Acc. Chem. Res.* **2013**, *46*, 160–170.
15. Pénicaud, A.; Drummond, C. Deconstructing Graphite: Graphenide Solutions. *Acc. Chem. Res.* **2013**, *46*, 129–137.
16. Sarkar, S.; Bekyarova, E.; Haddon, R. C. Chemistry at the Dirac Point: Diels-Alder Reactivity of Graphene. *Acc. Chem. Res.* **2013**, *45*, 673–682.
17. Quintana, M.; Montellano, A.; Del Rio Castillo, A. E.; Tendeloo, G. V.; Bittencourt, C.; Prato, M. Selective Organic Functionalization of Graphene Bulk or Graphene Edges. *Chem. Commun.* **2011**, *47*, 9330–9332.
18. Quintana, M.; Spyrou, K.; Grzelczak, M.; Browne, W. R.; Rudolf, P.; Prato, M. Functionalization of Graphene *via* 1,3-Dipolar Cycloaddition. *ACS Nano* **2010**, *4*, 3527–3533.
19. Sinitskii, A.; Dimiev, A.; Corley, D. a.; Fursina, A. a.; Kosynkin, D. V.; Tour, J. M. Kinetics of Diazonium Functionalization of Chemically Converted Graphene Nanoribbons. *ACS nano* **2010**, *4*, 1949–54.
20. Lomeda, J. R.; Doyle, C. D.; Kosynkin, D. V.; Hwang, W.-F.; Tour, J. M. Diazonium Functionalization of Surfactant-Wrapped Chemically Converted Graphene Sheets. *J. Am. Chem. Soc.* **2008**, *130*, 16201–16206.
21. Jin, Z.; Mcnicholas, T. P.; Shih, C.-j.; Wang, Q. H.; Paulus, G. L. C.; Hilmer, A. J.; Shimizu, S.; Strano, M. S. Click Chemistry on Solution-Dispersed Graphene and Monolayer CVD Graphene. *Chem. Mater.* **2011**, 3362–3370.
22. Sharma, R.; Baik, J. H.; Perera, C. J.; Strano, M. S. Anomalously Large Reactivity of Single Graphene Layers and Edges toward Electron Transfer Chemistries. *Nano Lett.* **2010**, *10*, 398–405.
23. Niyogi, S.; Bekyarova, E.; Hong, J.; Khizroev, S.; Berger, C.; Heer, W. D.; Haddon, R. C. Covalent Chemistry for Graphene Electronics. *J. Phys. Chem. Lett.* **2011**, *2*, 2487–2498.
24. Niyogi, S.; Bekyarova, E.; Itkis, M. E.; Zhang, H.; Shepperd, K.; Hicks, J.; Sprinkle, M.; Berger, C.; Lau, C. N.; Deheer, W. a.; *et al.* Spectroscopy of Covalently Functionalized Graphene. *Nano Lett.* **2010**, *10*, 4061–4066.
25. Choi, J.; Kim, K.-j.; Kim, B.; Lee, H.; Kim, S. Covalent Functionalization of Epitaxial Graphene by Azidotrimethylsilane. *J. Phys. Chem. C* **2009**, *113*, 9433–9435.
26. Quintana, M.; Vazquez, E.; Prato, M. Organic Functionalization of Graphene in Dispersions. *Acc. Chem. Res.* **2013**, *46*, 138–148.
27. Chattopadhyay, J.; Sadana, A. K.; Liang, F.; Beach, J. M.; Xiao, Y.; Hauge, R. H.; Billups, W. E. Carbon Nanotube Salts. Arylation of Single-Wall Carbon Nanotubes. *Org. Lett.* **2005**, *7*, 4067–4069.
28. Bahr, J. L.; Tour, J. M. Highly Functionalized Carbon Nanotubes Using in Situ Generated Diazonium Compounds. *Chem. Mater.* **2001**, *13*, 3823–3824.
29. Gebhardt, B.; Syrgiannis, Z.; Backes, C.; Graupner, R.; Hauke, F.; Hirsch, A. Carbon Nanotube Sidewall Functionalization with Carbonyl Compounds--Modified Birch Conditions Vs the Organometallic Reduction Approach. *J. Am. Chem. Soc.* **2011**, *133*, 7985–7995.
30. Dreyer, D. R.; Park, S.; Bielawski, C. W.; Ruoff, R. S. The Chemistry of Graphene Oxide. *Chem. Soc. Rev.* **2010**, *39*, 228–240.
31. Compton, O. C.; Nguyen, S. T. Graphene Oxide, Highly Reduced Graphene Oxide, and Graphene: Versatile Building Blocks for Carbon-Based Materials. *Small* **2010**, *6*, 711–723.
32. Eigler, S.; Dotzer, C.; Hirsch, A.; Enzelberger, M.; Muller, P. Formation and Decomposition of CO_2 Intercalated Graphene Oxide. *Chem. Mater.* **2012**, *24*, 1276–1282.
33. Eigler, S.; Dotzer, C.; Hirsch, A. Visualization of Defect Densities in Reduced Graphene Oxide. *Carbon* **2012**, *50*, 3666–3673.
34. Ortolani, L.; Catheline, A.; Morandi, V.; Pénicaud, A. Transmission Electron Microscopy Study of Graphene Solutions. In *Graphita 2011*; Ottaviano, L., Morandi, V., Eds.; Springer: Berlin, Heidelberg, 2012; pp 157−163.
35. Wang, Q. H.; Jin, Z.; Kim, K. K.; Hilmer, A. J.; Paulus, G. L. C.; Shih, C.-J.; Ham, M.-H.; Sanchez-Yamagishi, J. D.; Watanabe, K.; Taniguchi, T.; *et al.* Understanding and Controlling the Substrate Effect on Graphene Electron-Transfer Chemistry *via* Reactivity Imprint Lithography. *Nat. Chem.* **2012**, *4*, 724–732.
36. Dresselhaus, M. S.; Jorio, A.; Hofmann, M.; Dresselhaus, G.; Saito, R. Perspectives on Carbon Nanotubes and Graphene Raman Spectroscopy. *Nano Lett.* **2010**, *10*, 751–758.
37. Robinson, J. T.; Schmucker, S. W.; Diaconescu, C. B.; Long, J. P.; Culbertson, J. C.; Ohta, T.; Friedman, A. L.; Beechem, T. E. Electronic Hybridization of Large-Area Stacked Graphene Films. *ACS Nano* **2012**, *7*, 637–644.
38. Das, A.; Pisana, S.; Chakraborty, B.; Piscanec, S.; Saha, S. K.; Waghmare, U. V.; Novoselov, K. S.; Krishnamurthy, H. R.; Geim, A. K.; Ferrari, A. C.; *et al.* Monitoring Dopants by Raman Scattering in an Electrochemically Top-Gated Graphene Transistor. *Nat. Nanotechnol.* **2008**, *3*, 210–215.
39. Malard, L. M.; Pimenta, M. A.; Dresselhaus, G.; Dresselhaus, M. S. Raman Spectroscopy in Graphene. *Phys. Rep.* **2009**, *473*, 51–87.
40. Cançado, L. G.; Jorio, A.; Ferreira, E. H. M.; Stavale, F.; Achete, C. A.; Capaz, R. B.; Moutinho, M. V. O.; Lombardo, A.; Kulmala, T.; Ferrari, A. C. Quantifying Defects in Graphene *via* Raman Spectroscopy at Different Excitation Energies. *Nano Lett.* **2011**, *11*, 3190–3196.
41. Lucchese, M. M.; Stavale, F.; Ferreira, E. H. M.; Vilani, C.; Moutinho, M. V. O.; Capaz, R. B.; Achete, C. a.; Jorio, a. Quantifying Ion-Induced Defects and Raman Relaxation Length in Graphene. *Carbon* **2010**, *48*, 1592–1597.
42. Ferrari, A. C.; Meyer, J.; Scardaci, V.; Casiraghi, C.; Lazzeri, M.; Mauri, F.; Piscanec, S.; Jiang, D.; Novoselov, K.; Roth, S.; *et al.* Raman Spectrum of Graphene and Graphene Layers. *Phys. Rev. Lett.* **2006**, *97*, 187401.
43. Pisana, S.; Lazzeri, M.; Casiraghi, C.; Novoselov, K. S.; Geim, a. K.; Ferrari, A. C.; Mauri, F. Breakdown of the Adiabatic Born-Oppenheimer Approximation in Graphene. *Nat. Mater.* **2007**, *6*, 198–201.
44. Ferrari, A. C. Raman Spectroscopy of Graphene and Graphite: Disorder, Electron−Phonon Coupling, Doping and Nonadiabatic Effects. *Solid State Commun.* **2007**, *143*, 47–57.
45. Hof, F.; Bosch, S.; Englert, J. M.; Hauke, F.; Hirsch, A. Statistical Raman Spectroscopy: A Method for the Characterization of Covalently Functionalized Single-Walled Carbon Nanotubes. *Angew. Chem., Int. Ed.* **2012**, *51*, 11727–11730.
46. Liu, H.; Ryu, S.; Chen, Z.; Steigerwald, M. L.; Nuckolls, C.; Brus, L. E. Photochemical Reactivity of Graphene. *J. Am. Chem. Soc.* **2009**, *131*, 17099–17101.
47. Thomsen, C.; Reich, S. Double Resonant Raman Scattering in Graphite. *Phys. Rev. Lett.* **2000**, *85*, 5214–5217.
48. Maultzsch, J.; Reich, S.; Thomsen, C. Double-Resonant Raman Scattering in Graphite: Interference Effects, Selection Rules, and Phonon Dispersion. *Phys. Rev. B* **2004**, *70*, 155403.

49. Ferrari, A.; Robertson, J. Resonant Raman Spectroscopy of Disordered, Amorphous, and Diamondlike Carbon. *Phys. Rev. B* **2001**, *64*, 075414.
50. Pimenta, M. A.; Dresselhaus, G.; Dresselhaus, M. S.; Cancado, L. G.; Jorio, A.; Saito, R. Studying Disorder in Graphite-Based Systems by Raman Spectroscopy. *Phys. Chem. Chem. Phys.* **2007**, *9*, 1276–1291.